# Supporting Information

## Strong strain gradients and phase coexistence at the metal-insulator transition in $VO_2$ epitaxial films

Laura Rodríguez[1], Felip Sandiumenge[2], Carles Frontera[2], José Manuel Caicedo[1], Jessica Padilla[1], Gustau Catalán[1,3], and José Santiso[1,1]

[1] *Catalan Institute of Nanoscience and Nanotechnology, ICN2, CSIC and The Barcelona Institute of Science and Technology (BIST), Campus UAB, 08193 Bellaterra, Barcelona. Spain.*

[2] *Institut de Ciència de Materials de Barcelona (ICMAB-CSIC). Campus UAB, 08193 Bellaterra, Catalonia. Spain.*

[3] *ICREA - Institució Catalana de Recerca i Estudis Avançats, 08010 Barcelona, Catalonia. Spain*

**Supporting information file contains the following paragraphs:**

A. 3D reciprocal space maps of representative *hkl* reflections (**Figure S1**)
B. Projections of 3D reciprocal space maps (synchrotron radiation) at larger span of temperatures (from 25 ºC to 50 ºC, 5 ºC steps) for reflections 002 (**Figure S2**), 112 (**Figure S3**), 1/2 0 3/2 (**Figure S4**) and 101 (**Figure S5**).
C. Maps measured with lab diffractometer on 120 nm sample (**Figure S6**).
D. Details of the calculation of cell parameters, tilt and shear angles (**Figure S7**).
E. Matching between different close planes from bulk R and M1 structures (**Figure S8** and **Table S1**).
F. Additional comments about microcrack formation (**Figure S9**).
G. Comments about the Micro-Raman analysis of the epitaxial films (**Figure S10**).

[1] *Corresponding Author*: José Santiso López
Catalan Institute of Nanoscience and Nanotechnology, ICN2, CSIC and The Barcelona Institute of Science and Technology (BIST),
Campus UAB, 08193 Bellaterra, Barcelona. Spain.
Email: jose.santiso@icn2.cat
Orcid: 0000-0003-4274-2101.
Phone: +34 937373634

## A. 3D reciprocal space maps of representative *hkl* reflections

The following Figure S1 depicts the 3D reciprocal space maps measured with synchrotron radiation and the large angle 2D detector at 50 ºC for the most representative *hkl* reflections analysed in this study on the 120 nm thick $VO_2$ epitaxial film on $TiO_2$(001). Note that $VO_2$ film peaks show a considerable splitting following [110]*$_R$ and [1-10]*$_R$ directions in the reciprocal space (bisect planes between $Q_x$ and $Q_y$ axes, in red and yellow, respectively). The splitting of 002 reflection is symmetric and therefore it is exactly the same along [110]*$_R$ and [1-10]*$_R$ directions. This is why Figure 2 only shows one of the projections. In this representation the splitting asymmetry in the 112$_R$ film reflection is not as clear as in the plane cuts of Figure 2. The maps of 002$_R$ and 112$_R$ contain intense $TiO_2$ substrate peaks, while 1/2 0 3/2$_R$ reflection only shows film peaks. In this map only two split intensity spots are visible.

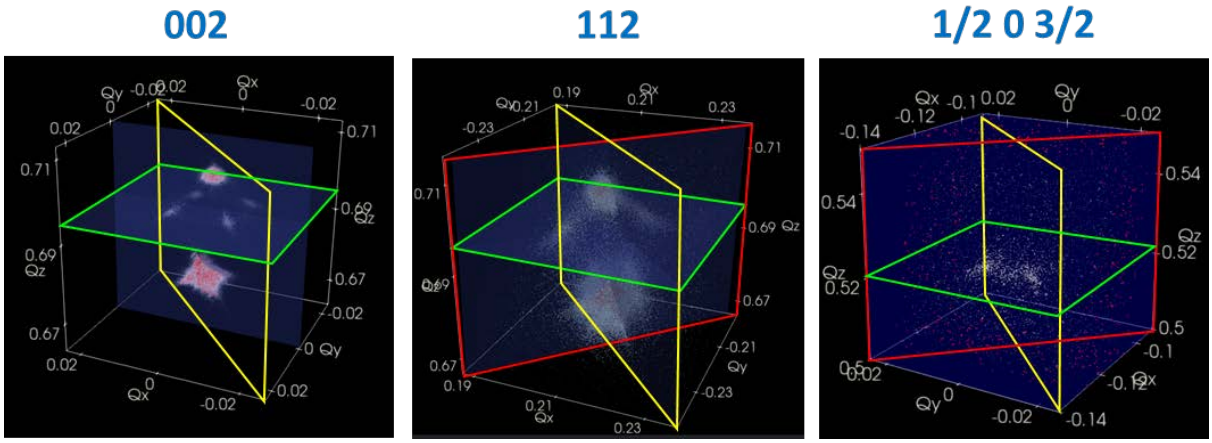


**Figure S1**. 3D reciprocal space maps of the 002$_R$, 112$_R$ and 1/2 0 3/2$_R$ reflections measured at 50 ºC for the 120nm thick $VO_2$ film deposited on $TiO_2$ (001). The plane cuts correspond to the 2D projections depicted in Figure 2 of the main manuscript. The plots show surfaces with equal intensity chosen to highlight the weak M1 split components.

**B. Measurements of 3D reciprocal space maps (synchrotron radiation) at larger span of temperatures (from 25 ºC to 50 ºC, 5 ºC steps)**

- **$002_R$ reflection ( = $40\overline{2}_{M1}$)**

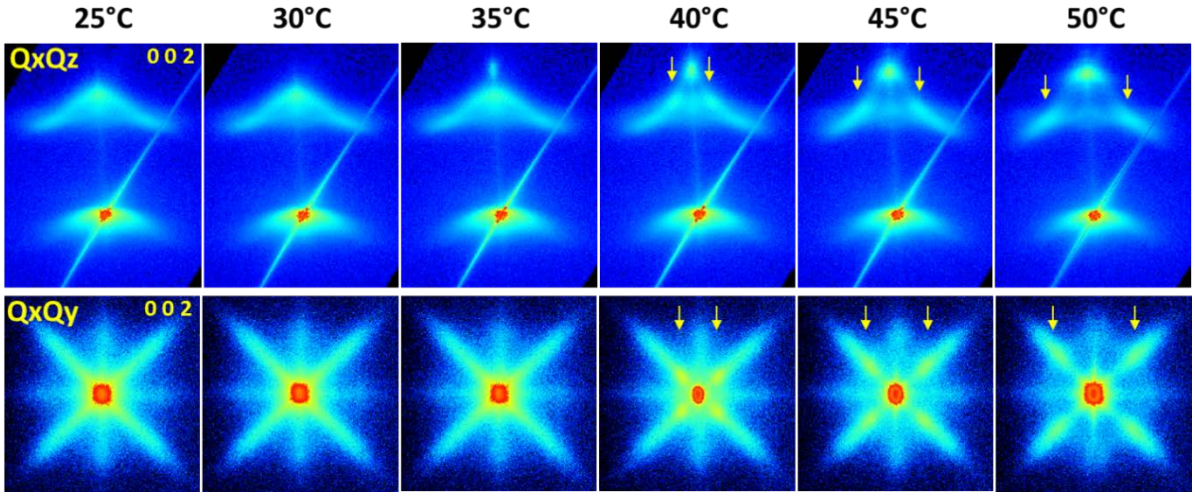


**Figure S2**. 2D Projections of reciprocal space 3D maps for $VO_2$ and $TiO_2$ tetragonal 002 reflections in the vertical $Q_xQ_z$ plane (top row) and horizontal $Q_xQ_y$ plane (bottom row). The horizontal projection contains only $VO_2$ film reflection. (The arrows indicate the split components) . Note that the vertical maps are projected along $Q_x$ axis (//[100]*$_R$) and not along $Q_{xy}$ (//[110]*$_R$ so they are slightly different to those depicted in Figure 2a.

- **$112_R$ reflection ( = $41\bar{1}M1$ ; $4\bar{1}\bar{3}M1$)**

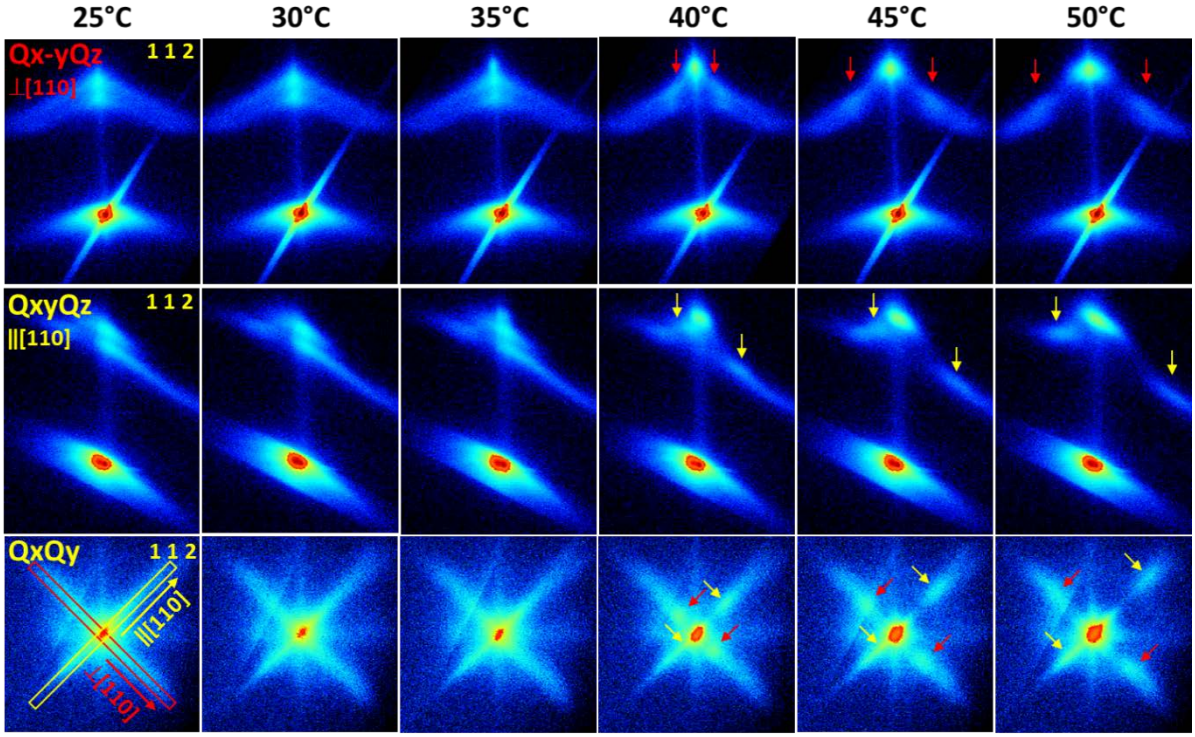


**Figure S3**. 2D Projections of reciprocal space 3D maps for $VO_2$ $112_R$ asymmetric reflections of $VO_2$ and $TiO_2$ in a vertical plane following [1-10]*$_R$ direction ($Q_{x\text{-}y}Q_z$ maps in top row), a vertical plane parallel to [110]*$_R$ direction ($Q_{xy}Q_z$ maps in middle row), and a horizontal $Q_xQ_y$ plane cut (bottom row). The horizontal projection contains only $VO_2$ film reflection (the arrows indicate the split components).

- **1/2 0 3/2$_R$ reflection ( = 6 0 $\bar{2}_{M1}$)**

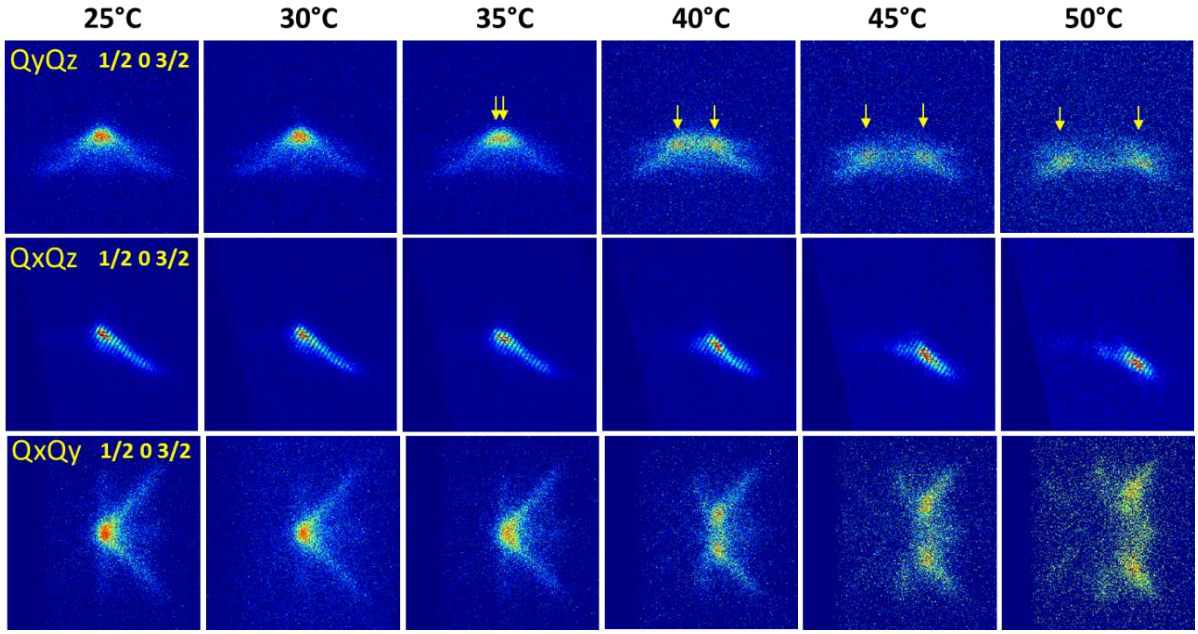


**Figure S4**. 2D Projections of 3D reciprocal space maps for 1/2 0 3/2$_R$ $VO_2$ reflection: vertical plane following [010]*R direction (top row); vertical plane parallel to [100]*$_R$ direction (middle row), and horizontal plane (bottom row). (The arrows indicate the split components). Note that in this representation the vertical maps are slightly different to that of Fig 2c which follows [110]*$_R$ direction. The $Q_yQ_z$ map shows (front) view of the two M1 split components, while the $Q_xQ_z$ map shows a lateral view where both split components overlap and only one component seem to appear.

**Additional reflections** in the same 120nm thick $VO_2$ film (same film as main manuscript)

- **$101_R$ reflection ( = $200_{M1}$ ; $20\bar{2}_{M1}$ ; $21\bar{1}_{M1}$)**

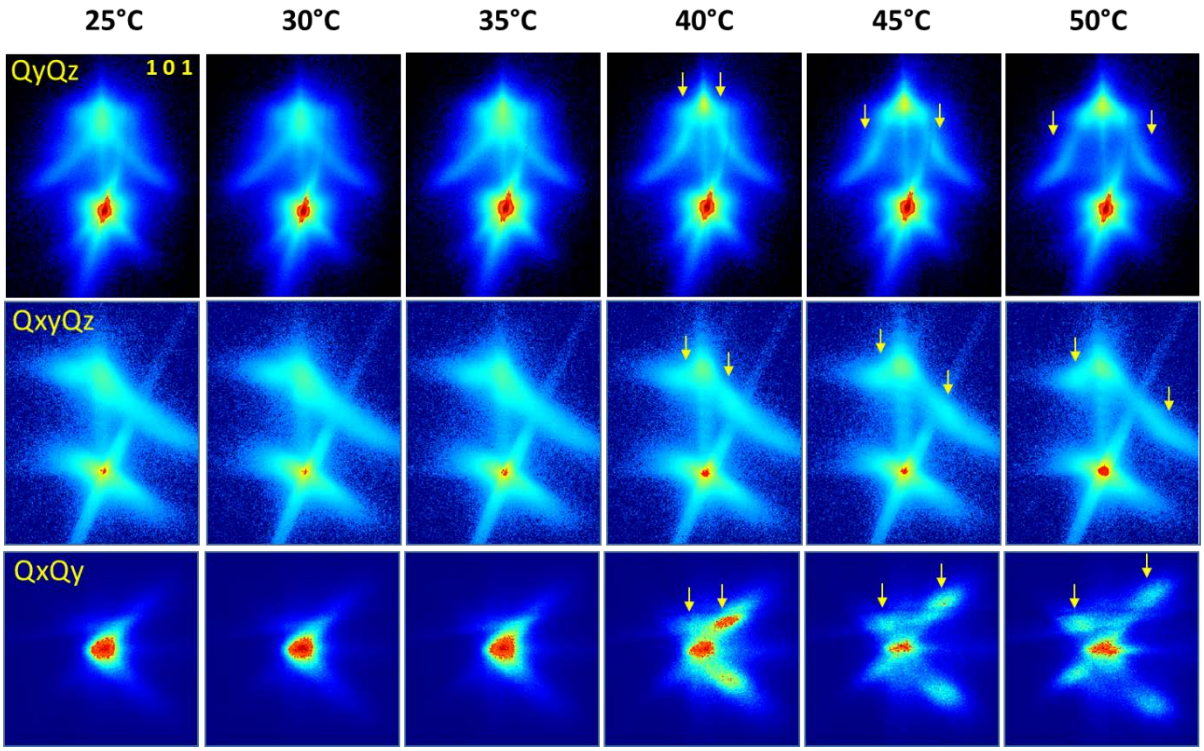


**Figure S5**. RSMs of $101_R$ reflections in vertical $Q_yQ_z$ (top), $Q_{xy}Q_z$ (middle) projections and horizontal $Q_xQ_y$ projection (bottom) for the same 120nm thick $VO_2$ film. [The horizontal projection only contains $VO_2$ signal. $TiO_2$ substrate signal has been cut out to avoid large overlap]

As in other HKL reflections (described in the main manuscript) the M1 signal splits in four components forming a distorted cross pattern in $Q_xQ_y$ following $[110]^*_R/[1\text{-}10]^*_R$ directions. These components are also displaced in $Q_z$. The two reflections close to the central ($Q_x$,$Q_y$) position in the map (the position of the $TiO_2$ substrate component as well as of R component), which are clearly resolved in the horizontal map, show a $Q_z$ very close to that of R component. This makes it difficult to resolve in the standard $Q_yQ_z$ projection of the vertical RSM (top row). The middle row corresponds to a vertical slice cut $Q_{xy}Q_z$ of the map following the direction $[110]^*_R$, which makes easier to resolve the different $Q_z$ positions of the M1 components. The arrangement of the different componentsis fully consistent with the described model of domain rotation and uniaxial compression (Figure 3 in main text).

## C. Maps measured with lab diffractometer on 120nm sample

The following maps, in Figure S6, for reflections $002_R$, $112_R$, and $103_R$ at different temperatures were measured at the lab diffractometer with 4-angle goniometer and linear detector, and were used to calculate the cell parameters variation of M1 and R phases.. Note that reflection 002R was measured either at $\phi=0^o$ or $45^o$ ($\phi$ azimuth angle, corresponds to the rotation in the plane of the sample). These maps correspond to projections either along $[100]^*_R$ or $[110]^*_R$ directions, respectively. As observed in the 3D maps of the reflections in the main text the splitting of M1 phase into several orientation variants produces an "inverted-V" shape of the M1 component in the maps.

Maps of $112_R$ reflection can only be measured in a conventional 4-angle goniometer at the equivalent $\phi=45^o$, and therefore, they correspond to the $[110]^*_R$ projections of the 3D maps in Figure 2b in the main manuscript (central row). Without the 3D measurement the fine structure in the perpendicular direction would have remained not observed.

The maps of $103_R$ reflection are measured at $\phi=0^o$ and, therefore, they correspond to a projection along $[100]^*_R$ direction. Since the M1 components are split along $[110]^*_R/[1\text{-}10]^*_R$ directions the progressive splitting with temperature brings the M1 reflections out from the measured region (centered in average R component). This brings some error in the estimate of the cell parameters for this reflection. Despite these limitations the measurement has been quite consistent for all reflections as evidenced by the cell parameters shown in Figure 5.

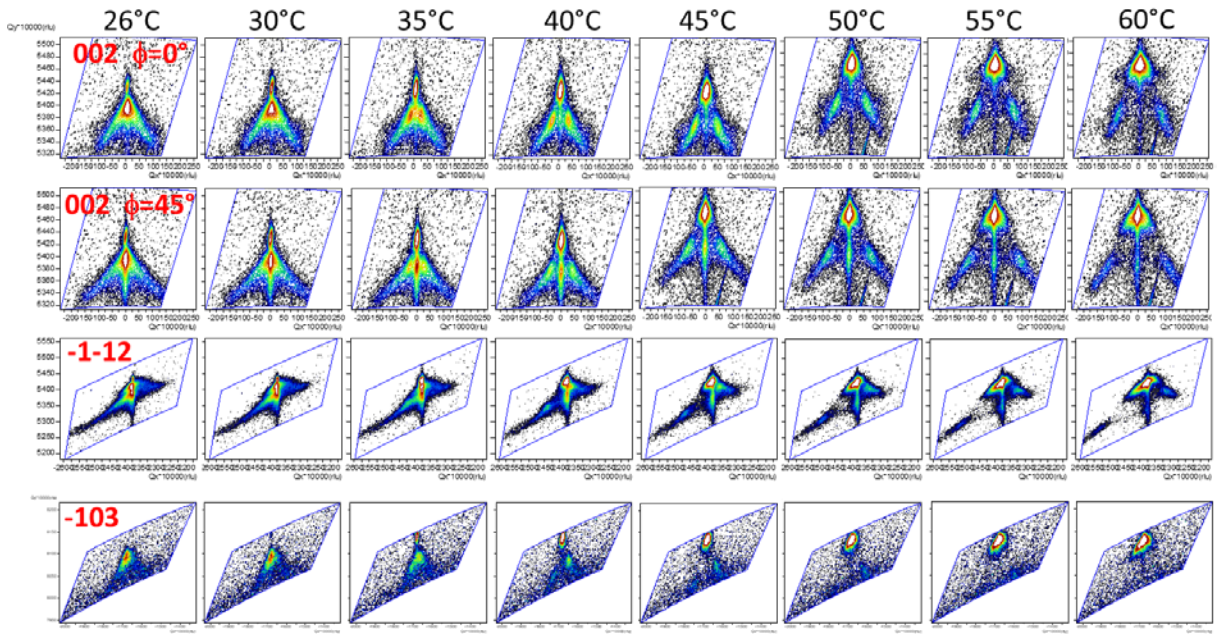


**Figure S6**. Reciprocal space maps measured with lab diffractometer (4-angle goniometer and linear detector) on 120 nm thick $VO_2$/ $TiO_2$ (001) epitaxial film for reflections $002_R$ (at $\phi$= 0° and 45°), $-1-12_R$ and $-103_R$. (Intensity in logarithmic scale). [The (–) sign of the non-symmetric reflections indicates the choice of the high-incidence vs high-exit angle geometry of the measurement].

## D. Details of the calculation of cell parameters, tilt and shear angles

For tilted M1 domains the lattice parameters were calculated from the average position of the two opposite split components (taken as pairs of opposite tilt), while tilt angle component was calculated from the width of the splitting of the different reflections. As an example, Figure S7 shows a more detailed view of $002_R$, $112_R$ and $103_R$ maps measured at T= 45 ºC. For $002_R$ maps two separate measurements were carried out at $\phi$=0° and 45º, corresponding to projections along $[100]^*_R$ and $[110]^*_R$ directions, respectively. In the 002 map at $\phi$=45º R phase has one single component, while corresponding $40\text{-}2_{M1}$ reflection (equivalent to $002_R$ in pseudo-rutile representation) shows three components: two split components (resulting from tilted domains) at opposite angle, and one central component. In fact, the central component is the projection of a double reflection with tilt perpendicular to the view. The 3D view in Figure S1 clearly shows the appearance of 4 symmetric components, corresponding to M1 domains tilted along each of the $<110>^*_R$ equivalent directions. Then, the projection parallel to $[110]^*_R$ should show only 3 components. In this case, the out-of-plane $d_{001}$ parameter and tilt angle can be calculated from the reciprocal space position of the titled components. A similar situation occurs for the $112_R$ map. R component consists of one single peak, while M1 shows three components, corresponding to equivalent $41\text{-}1_{M1}$ and $4\text{-}1\text{-}3_{M1}$ reflections. In this case the M1 out-of-plane and one set of in-plane cell parameters can be easily calculated from the average positions of the titled components, while another set of in-plane parameters can be calculated from the central component (as well consisting of a projection of a double peak along the view direction). Unfortunately, in the lab diffractometer it is not easy to extract a section of the RSM in that direction to show the double peak (due to the large beam divergence in the axial plane when using long fine focus X-ray beam, as in the present measurements). That is one of the reasons the measurements were also performed in synchrotron line with a 2D detector, which allows for a 3D measurement of the RSMs. The M1 component rotation is extracted from the splitting of the tilted components, assuming a symmetric rotation (equal opposite tilt angles) around the average ($Q_x$,$Q_z$) position. In the 002 map at $\phi$= 0º there are only two components of $40\text{-}2_{M1}$ reflection. Each of these components corresponds to a double peak as expected for the four-fold splitting projected along the $[100]^*_R$ direction. Similarly, the $103_R$ reflection shows two titled components for M1, (corresponding to equivalent $60\text{-}2_{M1}$, and $61\text{-}3_{M1}$ reflections), along with the single component for R. The two M1 components are again a projection of a double peak exactly at the same ($Q_x$,$Q_z$) positions but different $Q_y$ (perpendicular to map cut). Domain rotation is extracted from the splitting of titled components at both sides of the average position.

Note that in this case the rotation angle is a projection along $[100]^*_R$ direction, and therefore, to be able to compare it to the rotation measured along $[110]^*_R$ it is necessary to multiply by a factor $\times\sqrt{2}$. Since a pure rotation of a tetragonal structure should not affect the corresponding $d_{HKL}$ values, the difference in $d_{HKL}$ (after rotation is corrected) for the two opposite components of $112_R$ of M1 domains corresponds to the shear angle distortion of the monoclinic structure. In this way shear angle could be decoupled from pure tilting angle.

The extracted values for R and M1 cell parameters, as well as domain rotation and shear angles, by using this procedure are depicted in Figure 5.

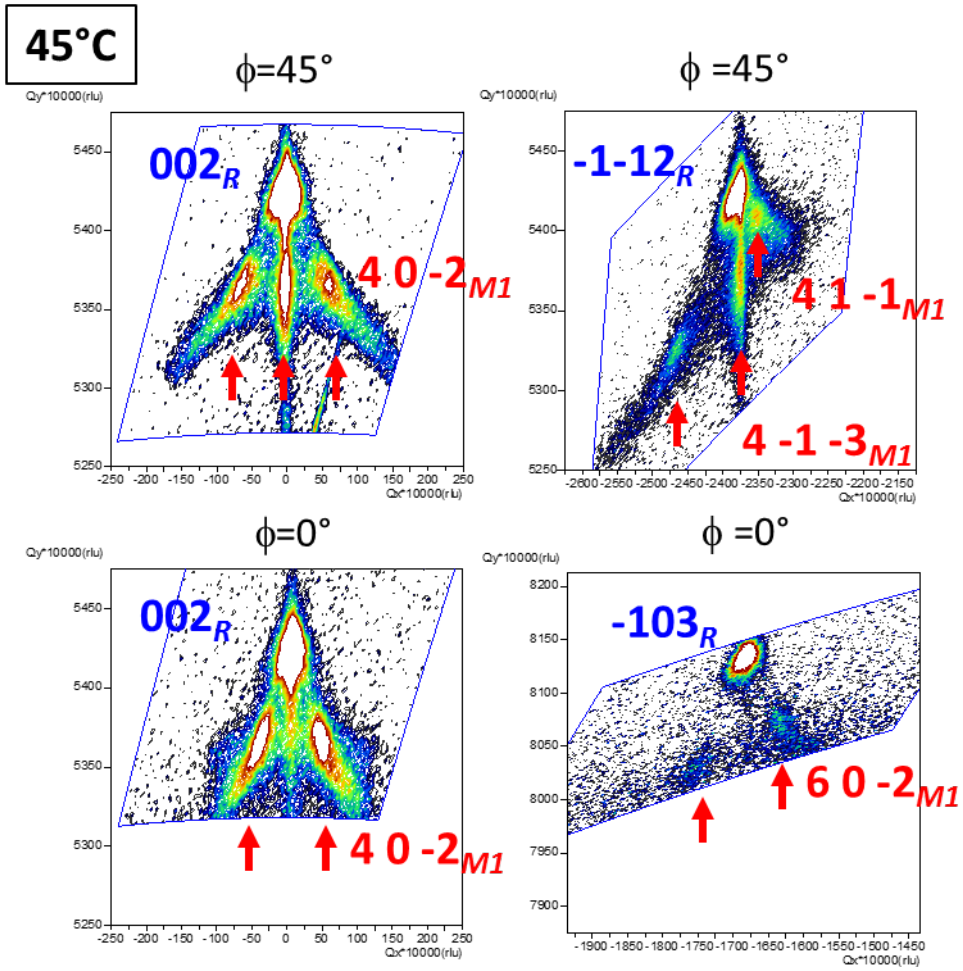


**Figure S7**. Detail of the reciprocal space maps of $002_R$ (at ϕ= 0° and 45º), $112_R$ and $103_R$ film reflections measured at 45ºC for the 120nm thick $VO_2$/ $TiO_2$ (001) sample. The arrows indicate the different split components of M1 domains, along with their corresponding indexing in $P2_1/c$ space group.

## E. Matching between different close planes from bulk R and M1 structures

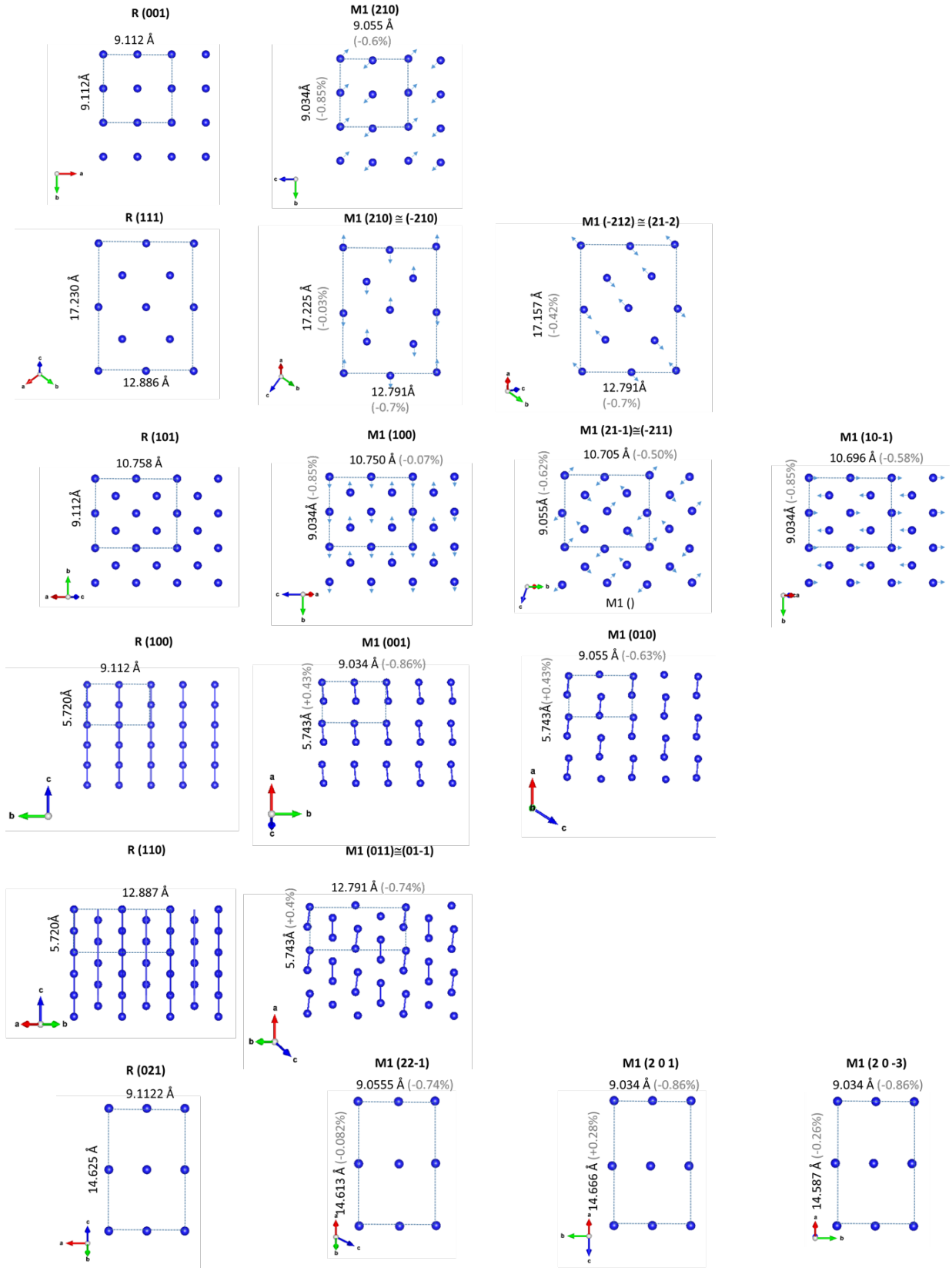


**Figure S8**. Principal common planes of bulk R and M1 structures, along with corresponding distances to calculate their mismatch.

By taking the reported structures of $VO_2$ Rutile (R) (tetragonal, $P4_2/mnm$) $a$=4.5561 Å, $c$=2.8598 Å, and M1 (Monoclinic, $P2_1/c$) $a$= 5.7430 Å, $b$=4.5170 Å, $c$= 5.37500 Å, β= 122.61º, (Andersson et al, ref [37] in main manuscript) it is possible to calculate the mismatch between possible contact planes of R and M1 structures close to the epitaxial orientation of the films. Figure S8 indicates the distances between V atoms in the corresponding plane along two orthogonal directions. The lower symmetry of the Monoclinic phase makes that for each HKL planes of rutile there are several possible planes of M1 (in the same row).

For each plane the shift in individual V atoms with respect to the tetragonal phase is indicated by small arrows. These shifts affect the periodicity along the orthogonal directions in each plane. The relative difference in V-V distances between M1 and R was calculated for a periodic supercell with quasi-coincident sites (indicated with dashed lines). The slight shear distortion was not taken into account for the calculation. The linear mismatch % along the two orthogonal directions ($\varepsilon_1$ and $\varepsilon_2$) are listed in the following Table S1.

**Table S1**. Calculated linear mismatch along orthogonal directions for the main common crystal planes of R and M1 bulk structures

| crystal planes | | linear mismatch | |
|---|---|---|---|
| Rutile, R | Monoclinic, M1 | $\varepsilon_1$ [%] | $\varepsilon_2$ [%] |
| $(001)_R$ | $(210)_{M1}$ | -0.6 | -0.85 |
| $(100)_R$ | $(001)_{M1}$ | -0.86 | +0.43 |
| | $(010)_{M1}$ | -0.63 | +0.43 |
| $(110)_R$ | $(011)_{M1}$, $(01\text{-}1)_{M1}$ | -0.74 | -0.4 |
| $(101)_R$ | $(100)_{M1}$ | -0.07 | -0.85 |
| | $(21\text{-}1)_{M1}$, $(\text{-}211)_{M1}$ | -0.50 | -0.62 |
| | $(10\text{-}1)_{M1}$ | -0.58 | -0.85 |
| $(111)_R$ | $(210)_{M1}$, $(\text{-}210)_{M1}$ | -0.7 | -0.03 |
| | $(\text{-}212)_{M1}$, $(21\text{-}2)_{M1}$ | -0.7 | -0.42 |
| $(021)_R$ | $(22\text{-}1)_{M1}$ | -0.74 | -0.08 |
| | $(201)_{M1}$ | -0.86 | +0.28 |
| | $(20\text{-}3)_{M1}$ | -0.86 | -0.26 |

From the listed values it is clear that the best match between R and M1 bulk phases is produced for $(111)_R$ // $(210)_{M1}$ or $(-210)_{M1}$ planes, mostly because of the very small mismatch along the vertical direction ($\varepsilon_2$). Still, there are some other interface orientations that result in close mismatch values, such as $(101)_R$//$(100)_{M1}$ and $(021)_R$//$(22\text{-}1)_{M1}$, but they did not reproduce the domain arrangement experimentally observed. It is likely that the strained values of R domains in the epitaxial films contribute further to favour the $(111)_R$//$(210)_{M1}$ in front of the rest.

## F. Additional comments about microcrack formation

Figure S9 shows surface morphology of $VO_2$/ $TiO_2$ (001) epitaxial films deposited by PLD with different thickness from 10 to 120 nm. Films with thickness below 15nm show flat morphology, while above that thickness the films start developing microcracks following $[110]_R$/$[1\text{-}10]_R$ in-plane directions (diagonals in the images). The microcrack linear density was roughly estimated from these images, and is shown in Figure S9 (bottom part). It progressively increases with film thickness, reaching a value of about 2 $\mu m^{-1}$ at 120nm. The error bars in the graph correspond to one $\sigma$ (standard deviation) in the distribution of microcrack spacing. The microcracks have been widely observed in epitaxial $VO_2$ films and seemingly result from the large increase in the elastic energy accumulated upon phase transition from R to M1 phase during cooling down after film deposition. In fully coherent epitaxial films, in absence of strain relaxation, the elastic energy of the strained films should be proportional to the substrate mismatch and the film thickness. Therefore, the increase in 0.78% to 1.5% mismatch between R and M1 phases (as estimated from the equilibrium reported values of in-plane cell parameters for c-axis oriented structures) almost doubles the elastic energy across the phase transition during cooling down. Therefore, if the sample is sufficiently thick it may surpass the elastic limit for defect formation, i.e. dislocation accumulation, and eventually leading to microcrack formation. This thickness limit has been proven to be between 10 and 15 nm for these films of $VO_2$/ $TiO_2$ (001). The thicker the films the higher the microcrack density as results of the accumulated elastic energy proportional to film thickness. Microcracks progress across the whole film thickness reaching the $TiO_2$ substrate affecting the strain relaxation of $VO_2$ regions in close proximity to the cracks. Since microcrack formation is dependent on kinetic parameters such as cooling/heating rate, as well as number of previous thermal cycles, a realistic comparative study of crack formation should be done at identical thermal history conditions, which was beyond this study.

The large crack spacing compared to the film thickness, 1.5 μm and 0.5 μm for the 60 nm and 120 nm thick films, respectively, makes that a sufficient proportion of the $VO_2$ film remains unaffected. The cracks therefore define a lateral strain relaxation distribution in addition to epitaxial strain induced by the growth on the $TiO_2$ substrate. This particular arrangement is manifested in the broadening of the phase transition compared to a homogeneous $VO_2$ material. It is known that strain lowers the phase transition temperature in $VO_2$ below the reported bulk value of about Tc ~68 ºC. Therefore, a $VO_2$ material with regions with a different strain state

should show different Tc's producing in average a broadening in apparent transition, and distinct regions with M1 and R phase during transition. This was described in a previous paper [Rodríguez et al. (2020). Self-Pixelation Through Fracture in $VO_2$ Thin Films. ACS Appl. Electron. Mater. 2020, 2, 5, 1433, reference [24] in main manuscript].)

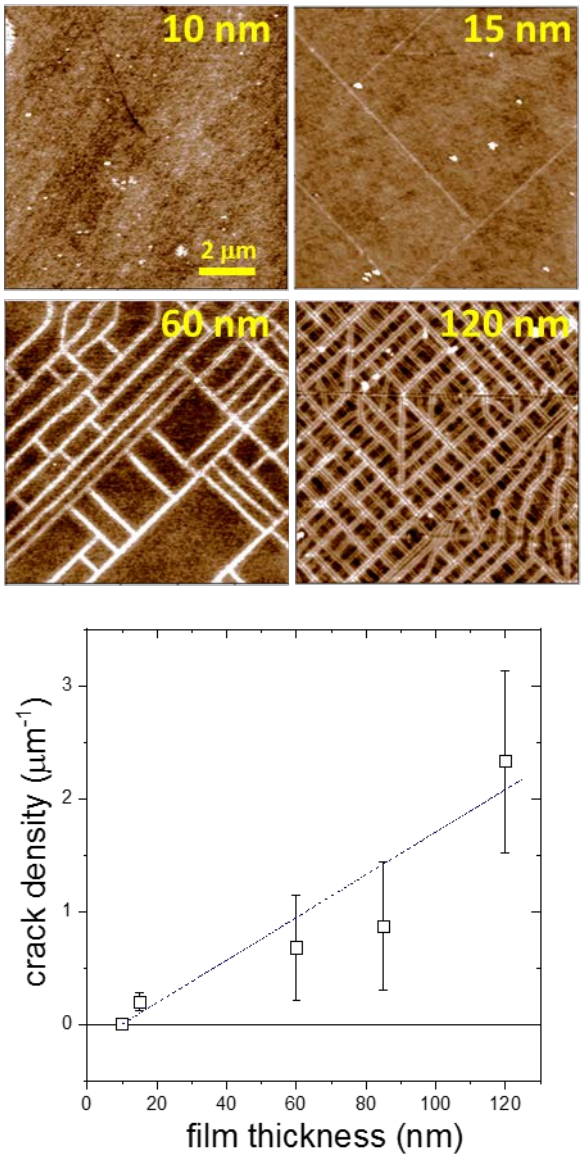


**Figure S9**. AFM topography images of $VO_2$ films with different thickness showing progressive crack formation. The lower panel shows density of cracks versus film thickness. (Error bars correspond to σ standard deviation)

## G. Comments about the Micro-Raman analysis of the epitaxial films.

As reported in several Raman spectroscopy studies carried out in $VO_2$ microcrystals (nanoplatelets) [see for instance: Atkin *et al.* 2012, or Strelcov *et al.* 2012] the blue-shift of $\omega_O$ phonon mode from 610 to 650 $cm^{-1}$ is typically used to distinguish the $VO_2$ phase transition M1→T→M2 (M1 phase $\omega_O$ <615 $cm^{-1}$; T within 615–646 $cm^{-1}$; M2 > 646 $cm^{-1}$; R phase does not contribute to any detectable Raman signal in this region).

In this study micro-Raman spectroscopy analysis was performed on the epitaxial films in order to identify the $VO_2$ structure as well as detecting its changes. The equipment used was a WITec Alpha 300r spectrometer working with a 488 nm (blue) and 633 nm (red) excitation wavelengths, and 1800 gr $nm^{-1}$ grating (resulting in a spectral resolution of 1/3 $cm^{-1}pixel^{-1}$). The laser spot was focused on the sample with a 100x objective, providing a lateral spatial resolution below 500 nm).

Figure S10 shows the measured spectra in separate regions of the sample at RT where the $VO_2$ stabilises in M1 and R phases, in densely cracked regions (fully relaxed, in orange) or fully strained far from crack regions (in blue), respectively. It is clear from the figure that the R regions, with fully $VO_2$ rutile structure, which is not expected to contribute to the Raman signal, showed a significant signal coming from the underlying $TiO_2$ substrate (comparable to that of $TiO_2$ bare substrate spectrum, in the insert). This signal from substrate was not possible to reduce even by accurate focusing on the film surface, since the penetration depth of the laser probe is very large compared to the $VO_2$ film thickness of about 100nm. Therefore, this overlap precluded any analysis by micro-Raman in the frequency region of the $\omega_O$ phonon mode.

Alternatively, in Fig. S10a the lower frequency region of the spectrum of M1 phase shows also peak signatures at 190 and 218 $cm^{-1}$ ($\omega_{v1}$ and $\omega_{v2}$ phonon modes, respectively) with smaller overlap with the $TiO_2$ substrate. In this region the differences between M1, T and M2 phases are reported to be more subtle, involving reduced frequency shifts and small relative intensity changes between $\omega_{v1}$ and $\omega_{v2}$ peaks [Atkin *et al.* 2012]. The maps in Figures SXb and c correspond respectively to intensity variations and frequency shift of the 190$cm^{-1}$ peak ($\omega_{v1}$ phonon mode) measured at RT in a region of 10x10$\mu m^2$. The dark region (in both maps)

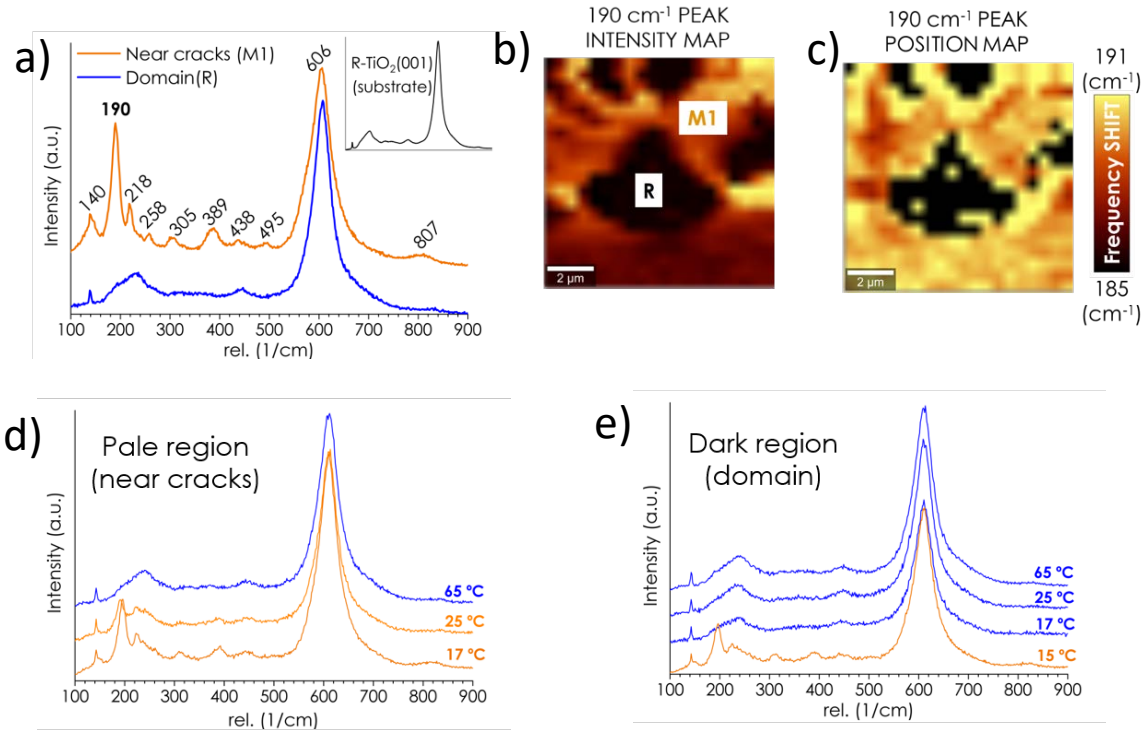


**Figure S10**. Micro-Raman analysis of the $VO_2$ epitaxial films. a) Full spectra in separate locations of the films with clear R and M1 domains, along with bare $TiO_2$ substrate Raman signal (insert); b) 10x10µm$^2$ map of the intensity at the $\omega_{v1}$ phonon mode at 190 cm$^{-1}$ frequency; c) map in the same 10x10µm$^2$ region of the frequency shift of the $\omega_{v1}$ phonon mode; d) full spectra measured at different temperatures across the transition in monoclinic region at RT, and e) in Rutile region at RT (note that first spectra with monoclinic features was obtained by cooling down below transition).

corresponds to the R phase (obviously no intensity, and no peak shift), while the bright regions show slightly different levels of intensity or peak shift. Indeed, these differences could be caused by the coexistence of M1, M2 or T phases, however, comparing Figures S10b and c we did not find a clear correspondence between regions of lower intensity of $\omega_{v1}$ and larger peak shift as it would be expected for the M1→T→M2 transformation. We believe that other factors, such as variable degrees of phase coexistence through the thickness of the film and strain can contribute to the observed inhomogeneities.

Even more challenging is the micro-Raman analysis at variable temperature during heating-cooling cycles. Maintaining the necessary spatial resolution results in a poorer frequency resolution, which did not allow to discern intermediate states between the M1 and R

phases. Figures S10d and e show the evolution of the micro-Raman spectra in different regions with originally M1 phase at low T (near cracks) or R phase (far from crack regions), respectively. Although there is a clear evolution of the spectra between the monoclinic and tetragonal states, rather than an abrupt change, again the spectra did not reveal clear signatures of the M2 or T phases. As suggested above, this may mean that the M2 and T phases are intermixed through the film thickness in the probed volume so their features cannot be clearly discerned. More accurate measurements with longer acquisition times should be performed in order to analyse the subtle features of $\omega_{v1}$ and $\omega_{v2}$ phonon modes to probe the spatial distribution of M2 and T phases.

J.M. Atkin, S. Berweger, E.K. Chavez, M.B. Raschke, J. Cao, W. Fan, J. Wu, Strain and temperature dependence of the insulating phases of $VO_2$ near the metal-insulator transition, Phys. Rev. B. 85 (2012) 20101. https://doi.org/10.1103/PhysRevB.85.020101.

E. Strelcov, A. Tselev, I. Ivanov, J.D. Budai, J. Zhang, J.Z. Tischler, I. Kravchenko, S. V Kalinin, A. Kolmakov, Doping-Based Stabilization of the M2 Phase in Free-Standing $VO_2$ Nanostructures at Room Temperature, Nano Lett. 12 (2012) 6198–6205. https://doi.org/10.1021/nl303065h